Frequency metrology on the EF (1)Sigma(+)(g)<- X (1)Sigma(+)(g)(0,0) transition in H2, HD, and D2

Hannemann, S.; Salumbides, E.J.; Witte, S.; Zinkstok, R.T.; van Duijn, E.J.; Eikema, K.S.E.; Ubachs, W.M.G.

published in
Physical Review A. Atomic, Molecular and Optical Physics
2006

DOI (link to publisher)
10.1103/PhysRevA.74.062514

document version
Publisher's PDF, also known as Version of record

Frequency metrology on the $EF\ ^1\Sigma_g^+ \leftarrow X\ ^1\Sigma_g^+(0,0)$ transition in H_2, HD, and D_2

S. Hannemann, E. J. Salumbides, S. Witte, R. T. Zinkstok, E. -J. van Duijn, K. S. E. Eikema, and W. Ubachs
Laser Centre, Department of Physics and Astronomy, Vrije Universiteit, De Boelelaan 1081, 1081 HV Amsterdam, The Netherlands
(Received 11 October 2006; published 28 December 2006)

We present a frequency metrology study on the lowest rotational levels of the hydrogen $EF\ ^1\Sigma_g^+ \leftarrow X\ ^1\Sigma_g^+(0,0)$ two-photon transition near 202 nm. For this purpose, the fourth harmonic of an injection-seeded titanium:sapphire pulsed oscillator is employed in a Doppler-free REMPI-detection scheme on a molecular beam of hydrogen. A frequency comb laser is used to perform the absolute frequency calibration on the continuous-wave (CW) laser that injection-seeds the oscillator. Chirp-induced frequency differences between the output of the pulsed oscillator and the seeding light are monitored on-line, while possible systematic shifts related to the AC-Stark and Doppler effects are addressed in detail. The transition frequencies of the $Q(0)$ to $Q(2)$ lines in H_2 and D_2, and the $Q(0)$ and $Q(1)$ lines in HD are determined with an absolute accuracy at the 10^{-9} level.

DOI: 10.1103/PhysRevA.74.062514 PACS number(s): 33.20.−t, 42.62.Fi, 33.80.Rv, 39.30.+w

I. INTRODUCTION

Accurate determination of the dissocation and ionization energies of the hydrogen molecule and its isotopomers is an important test ground for quantum *ab initio* calculations on molecular systems [1,2]. The pioneers in the field, Kolos [3] and Wolniewicz [4] calculated values for the ionization potential of H_2 in the range 124 417.491–124 417.496 cm^{-1}, including adiabatic, nonadiabatic, relativistic, and radiative corrections to the Born-Oppenheimer results, believed to be accurate to within 0.01 cm^{-1}. The best theoretical value for the adiabatic dissociation limit is calculated to be 36 118.060 cm^{-1} [4].

At the experimental side, different approaches have been adopted to retrieve increasingly accurate values for these two key quantities. Balakrishnan *et al.* [5] directly excited the region near the $n=2$ dissociation threshold resulting in a value for the ground-state dissociation threshold $D_0(H_2)$ with an accuracy of 0.08 cm^{-1}. Eyler and McCormack showed that the region near the $n=2$ threshold is prone to spin-orbit and hyperfine effects as well as perturbations between several electronic states, yielding an irregular structure of many resonances near threshold [6] and later obtained a value for $D_0(H_2)$ in a two-step excitation process [7].

The ionization potential in hydrogen can be determined from direct one-photon excitation of the np Rydberg series and extrapolation to the series limit using multichannel quantum defect theory (MQDT). This approach was taken by Greetham *et al.* [8] to deduce a value for the ionization potential of HD. Alternatively, the ionization potential may be derived from a number of consecutive excitation steps bridging the gap between the $X\ ^1\Sigma_g^+$, $v=0$, $J=0$ ground state and the ionization limit. One such route was explored by De Lange *et al.* [9] who calibrated a high-lying vibrational level ($v=19$) in the $EF\ ^1\Sigma_g^+$ state and then connected to the ionization limit through the Fourier-transform infrared work on inter-Rydberg transitions by Jungen *et al.* [10] This scheme is fundamentally limited by the fact that a transition needs to be calibrated in the $B\ ^1\Sigma_u^+ \rightarrow X\ ^1\Sigma_g^+$ system, probing an upper state with a lifetime as short as 0.3 ns.

A promising multistep scheme involves calibration of the lowest $EF\ ^1\Sigma_g^+$, $v=0$ level (with a lifetime of 200 ns [11] and therewith allowing for precision spectroscopy), which can be reached in a two-photon transition allowing for Doppler-free excitation. This scheme was already explored some time ago by Glab and Hessler [12] and by Eyler and co-workers [13–16]. The concept of the multistep scheme is to determine the ionization potential from accurate calibration of the $EF\ ^1\Sigma_g^+$, $v=0$, $J=0$ level, subsequently excite the long-lived np Rydberg series, and then extrapolate this series to the limit with the aid of improved Fourier-transform infrared transitions between high-n levels [17] and by millimeter wave transitions between very high-n levels [18]. A recent reinvestigation of the $EF\ ^1\Sigma_g^+ \leftarrow X\ ^1\Sigma_g^+(0,0)$ two-photon transition by Eyler and co-workers constitutes an important improvement to this approach. Transition frequencies at an absolute accuracy of 0.008 cm^{-1} were obtained [19], that differed from earlier investigations by as much as three standard deviations. Such a discrepancy warrants an independent validation by alternative methods, and that is the purpose of the present study.

In the present experimental investigation, a pulsed laser source, tunable near 202 nm, is used for exciting the $Q(0)$ to $Q(2)$ lines of the $EF\ ^1\Sigma_g^+ \leftarrow X\ ^1\Sigma_g^+(0,0)$ band in H_2 and D_2, as well as the $Q(0)$ and $Q(1)$ lines in HD, in a two-photon Doppler-free resonance-enhanced multiphoton ionization (REMPI) scheme. Using a pulsed titanium:sapphire (Ti:sapphire) oscillator in the near infrared range, three stages of nonlinear conversion are required to attain deep-UV wavelengths [20]. The frequency metrology is performed on the output of the continuous-wave (CW) laser, that seeds the oscillator cavity of the pulsed laser system, by referencing against a home-built frequency comb laser [21,22]. As is known from pulsed-dye laser systems, the amplification process can induce frequency excursions during the temporal evolution of the pulse (known as frequency chirp), which may cause a net shift between the center frequency of the pulse and the carrier-frequency seeding the pulsed amplifier [23–25]. For the absolute calibration of the $Q(0)$, $Q(1)$, and $Q(2)$ transitions in the hydrogen $EF\ ^1\Sigma_g^+ \leftarrow X\ ^1\Sigma_g^+(0,0)$ band, we have performed extensive measurements on these chirp effects and corrected for them. Although the underlying physics of the chirp process is somewhat different (frequency

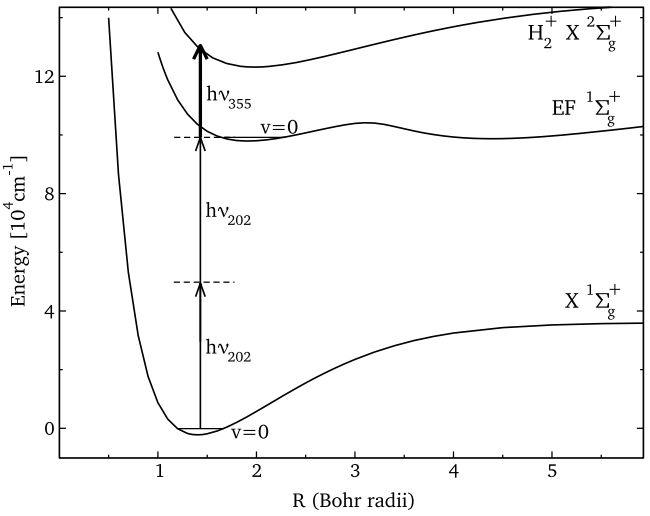

FIG. 1. Potential diagram of molecular hydrogen and the applied (2+1)-REMPI excitation scheme. The zero energy is identified with the ground state.

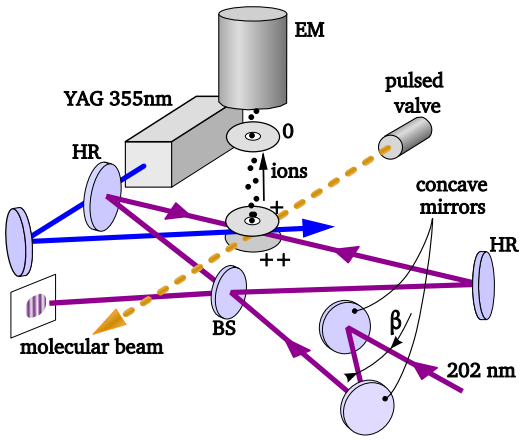

FIG. 2. (Color online) Experimental apparatus used for Doppler-free (2+1)-REMPI detection on a molecular beam. The pulsed valve injects the gas directly to the interaction chamber in a free jet expansion. The laser beam is collimated using a telescope consisting of concave mirrors. A pair of counterpropagating beams is aligned in a Sagnac interferometer using a beam splitter (BS) and highly reflective mirrors (HR). An auxiliary Nd:YAG laser operating at 355 nm serves to ionize the H_2 molecules excited to the *EF* state by the first laser.

mode-pulling in a resonator vs transient gain in a traveling-wave dye-amplifier) the phenomenology of the effect is similar. We followed strategies recently explored by White *et al.* [26,27] for determining chirp phenomena in an injection-seeded and pulsed optical parametric oscillator.

II. EXPERIMENTAL SETUP AND PROCEDURES

The $EF \leftarrow X$ two-photon resonances are detected using Doppler-free 2+1-REMPI. An excitation scheme including potential energy curves is given in Fig. 1. The essential ingredients of the experimental components and the measurement procedures are described in detail in the following sections: In Sec. II A, the geometrical layout is of a molecular gas jet perpendicularly crossing a set of counterpropagating laser beams with (2+1)-REMPI detection. A special interferometric alignment scheme was followed (based on the Sagnac geometry) to ensure exact overlap of the counterpropagating beams. Section II B describes a novel-design tunable deep-UV laser system operating at 202 nm, involving fourth harmonic generation of the amplified output of an injection-seeded pulsed Ti:sapphire oscillator. Section II C curves the absolute frequency calibration of the near-IR seeding light using a fs-laser frequency comb; Sec. II D, the assessment of the frequency chirp effect; Sec. II E; the assessment of possible shifts due to DC and AC-Stark effects; Sec. II F, discussion of possible effects of phase distortions introduced by the Kerr effect in the nonlinear upconversion stages; and Sec. II G, the integration of the three laser systems (the seed-laser, the pulsed oscillator, and the frequency comb laser) and the on-line chirp detection into a computer-controlled measurement system and the measurement procedures.

A. Doppler-free (2+1)-REMPI in a gas jet

A schematic overview of the molecular beam apparatus, including the excitation and time-of-flight (TOF) mass separation and detection zones is shown in Fig. 2. Molecular hydrogen is injected into the vacuum using a pulsed valve at a stagnation pressure of 3 bar. The TOF chamber and the interaction chamber are both differentially pumped to a pressure of 10^{-7} mbar, which rises to $\sim 10^{-6}$ mbar when the molecular beam is present. Under these conditions, essentially collision-free transition frequencies can be determined.

Although the technique of two-photon spectroscopy employing counterpropagating laser beams is known to be Doppler-free, a slight misalignment from an exact antiparallel geometry can lead to Doppler shifts. In the case of an angular mismatch $\delta \ll 1$, the effective Doppler shift is

$$\Delta\nu = \delta \frac{v}{\lambda} \tag{1}$$

at the two-photon level, where v is the velocity of the hydrogen molecules and λ the wavelength of the UV light used for two-photon excitation.

In order to minimize calibration uncertainties due to possible Doppler shifts, a collimated laser beam with ~ 1 mm diam at the interaction zone was used. Since the UV light output of the laser system is astigmatic, a concave mirror telescope (see Fig. 2) is aligned under a certain angle β, making use of the abberation effects on spherical mirrors and thus compensating for the astigmatism. In a first alignment scheme, the collimated light was sent to the interaction zone over a distance of 1.5 m, while a plain retroreflecting mirror placed inside the vacuum on a pivoting mirror mount was aligned such that the counter propagating beams are overlapped. During the alignment procedure, a pinhole of 0.5 mm diam was placed in the center of the forward-directed beam. An overlap accuracy between the counterpropagating beams of ~ 0.3 mrad is achieved corresponding to a Doppler-shift of ~ 2.5 MHz at the two-photon energy level. A different, interferometric method has been employed

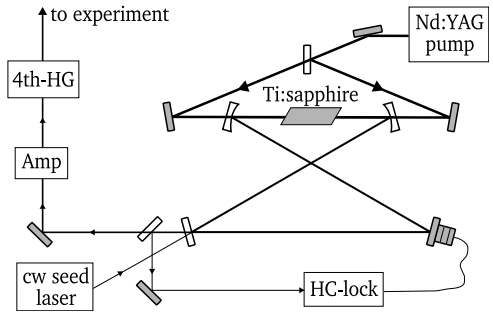

FIG. 3. Schematic layout of the laser system used. The laser resonator contains a Ti:sapphire crystal as single active optical element. The cavity length is locked using Hänsch-Couillaud (HC) scheme [29]. The amplifier system (Amp) is a multipass Ti:sapphire amplifier in a bowtie geometry. The fourth harmonic of the near-IR radiation is produced in three consecutive nonlinear crystals. For further details, see text and Sneep *et al.* [20]

during a later stage of the experiments based on the Sagnac geometry achieving a reproducible angular overlap of better than 0.1 mrad—or 0.8 MHz calibration uncertainty [28]. The stated uncertainty margins for the angular mismatch of the counterpropagating beams contain also an estimated contribution for the fact that the laser beam does not exhibit a perfectly Gaussian beam profile and features possible wavefront distortions.

The REMPI signals were induced either in a single-color (202 nm) excitation or in a two-color scheme. In the latter case, a strong UV-laser pulse (at 355 nm, the third harmonic of an auxiliary pulsed Nd:YAG laser) serves to ionize the resonantly excited population in the *EF* state. In particular for low-energy pulses ($<10\ \mu$J) of the resonant laser, the ion signal significantly increases in the two-color scheme. The UV-ionization pulse was delayed by ≈50 ns with respect to the excitation laser in order to avoid inducing AC-Stark and population depletion effects.

B. Deep-UV laser source

For the production of laser light at 202 nm, a tunable pulsed laser system at 10 Hz repetition rate is used. A schematic overview is given in Fig. 3. A gain-switched (passive) titanium:sapphire (Ti:sapphire) oscillator cavity is pumped by a Nd:YAG laser (Quanta Ray GCR 3). On injection seeding with the output of a CW Ti:sapphire ring laser (Coherent 899) at ~808 nm, the pulsed oscillator produces a Fourier-limited linewidth at the seed wavelength with a pulse energy of 0.5 mJ. The pulsed oscillator output can optionally be enhanced in a bowtie Ti:sapphire amplifier up to 30 mJ. In order to produce the fourth harmonic at 202 nm, three consecutive nonlinear upconversion stages—BBO crystals cut at appropriate type-I phase matching angles—are used [20]. The pulse energy at 202 nm is varied from zero to maximum output by rotating the polarization of the third harmonic light in front of the fourth harmonic mixing crystal using a λ/2 wave plate. The laser system reaches maximum output energies of 0.2 mJ/pulse at 202 nm.

The pulse duration and the bandwidth of the Ti:sapphire pulsed oscillator are found to depend strongly on the pulse energy of the pump laser. Under conditions of optimum power production (at 6 mJ/pulse pump energy, limited by damage of the reflective optics of the resonator) pulse lengths of 20 ns are readily obtained; under these conditions the bandwidth at deep UV wavelengths, after frequency quadrupling is ~40 MHz, as can be estimated from the linewidth of the obtained two-photon resonances. By limiting the pulse energy, the pulse duration can be extended to 40 ns. The bandwidth is then also reduced accordingly, by a factor of two. In the stage of the experiment where the final calibrations were performed, the Ti:sapphire pulsed oscillator was run in this mode delivering the narrowest linewidths.

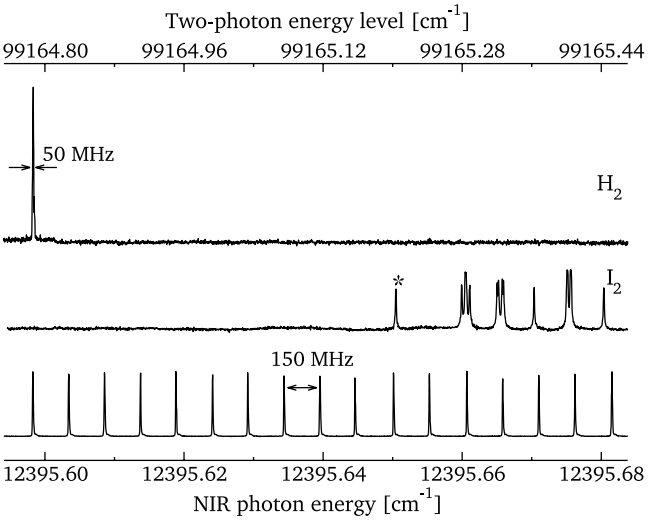

FIG. 4. Simultaneous spectral recording of the $EF\ ^1\Sigma_g^+ \leftarrow X\ ^1\Sigma_g^+(0,0)$ $Q(0)$ line of H_2 (via the one-color (2+1)-REMPI scheme), and a saturated I_2 spectrum as well as etalon markers produced at the fundamental wavelength. The line marked with an asterisk is the *t*-hyperfine component of the P(194) line in the $B\ ^3\Pi_u^+ - X\ ^1\Sigma_g^+(0,15)$ band of I_2 at 12 395.650 48 cm^{-1}, used as an absolute reference. The indicated linewidth on the H_2 resonance depends on the specific settings on the Ti:sapphire pulsed oscillator (pulse duration and bandwidth) and is given for the two-photon level frequency.

C. Absolute calibration procedures

Absolute calibration is performed on the CW seeding light from the Ti:sapphire ring laser. For an absolute calibration with a frequency comb the CW frequency has to be known within a fraction of the frequency spacing of neighboring modes in the comb, which is equal to the repetition rate of the frequency comb, in this case ≈75 MHz [22]. At the time, when these measurements were started, the transition frequencies of the $EF\ ^1\Sigma_g^+ \leftarrow X\ ^1\Sigma_g^+(0,0)$ were known to a 1σ accuracy of 0.003 cm^{-1} [30], which corresponds to 11 MHz accuracy in the infrared domain. In order to avoid any ambiguity on the specific mode, initial calibration experiments were performed with respect to the I_2 saturation standard in the near infrared. An example of a recording of the $Q(0)$ line in H_2 is shown in Fig. 4. The absolute frequency of the $Q(0)$ is found at 99 164.787(1) cm^{-1}—an accuracy of 4 MHz in the infrared—by referencing it to the

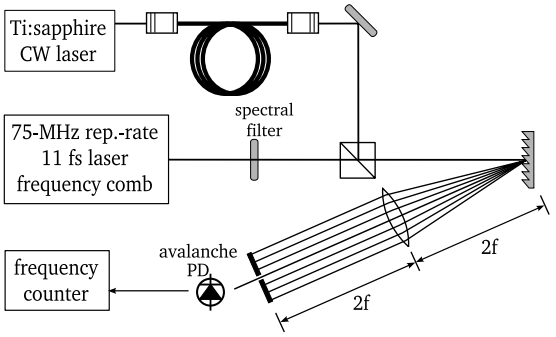

FIG. 5. Schematic view of the setup for the detection of the beatnote with the fs-laser frequency comb.

"*t*"-hyperfine component of the $P(194)$ line in the $B\,^3\Pi_u^+ - X\,^1\Sigma_g^+(0,15)$ band of I_2 at 12 395.65082 cm^{-1} [31], with inclusion of chirp corrections. According to the discussion of the AC-Stark shift in Sec. II E, its effect can be estimated to be ~2 MHz at the applied UV power levels for the precalibration. Hence, it can be neglected for the purpose of the mode identification.

For the final calibration measurements, part of the CW seed light is coupled through a 100 m single-mode optical fiber for transportation to another laboratory, where a phase and carrier-envelope stabilized femtosecond frequency comb laser is installed [21,22]. The CW-light is heterodyned with the output of this frequency comb in a setup as depicted in Fig. 5, and the radiofrequency (RF) beat note ν_{bn} is detected on an avalanche photodiode (PD). To increase the signal-to-noise ratio (s/n) on the photodetector, a grating and lens are used to disperse the spectrum of the frequency comb in a $4f$ configuration, so that a reduced number of modes is focused together with the CW mode on the PD. Typically, the beat-note detection reached a s/n of 45 dB. The two main parameters of the frequency comb are its carrier-envelope phase offset frequency ν_{ceo} and its repetition rate ν_{rep}. Both are locked against a Rubidium-clock standard, which is further referenced to the global positioning system (GPS). From the locking characteristics, the stability of each single frequency of the comb around 808 nm is estimated to be better than 100 kHz for the typical averaging times of 1 s.

The transition frequency ν_Q is measured by determining all radio frequencies involved, via

$$\nu_Q = \pm \nu_{bn} + \nu_{ceo} + n \times \nu_{rep}, \tag{2}$$

where the mode number n follows from the initial calibration using the I_2 saturated spectroscopy. The $\pm$ sign of the beat-note frequency ν_{bn} is determined by scanning the CW laser while monitoring the beat note between frequency comb and CW laser. When the CW laser is scanned to shorter wavelengths and the beat note increases accordingly, there is a plus sign, and when the beat note decreases there is a minus sign.

The beat note between the frequency comb and the CW laser is kept at ≈22 MHz over the entire scan for convenient electronic filtering. To achieve that, the repetition rate of the frequency comb is correspondingly scanned as the CW laser is tuned over the molecular resonance. The wavelength tuning was sufficiently slow to ensure that the comb mode is correctly identified. In effect, an absolute calibration is performed for every scan step. In Fig. 6, the counted beat notes between seeding light and frequency comb during a typical scan are shown. As pointed out before, the beat note remains constant at around 22 MHz over the entire scan. In order to obtain a result with reasonable statistics, at each scan step the beat note is counted ten times. Each single count is acquired within a time gate of 0.1 s, so that the beat-note counting takes 1 s per scan step. The given error bars depicted in the zoomed inlay are taken from the standard deviation of the ten beat-note frequency countings. Typical standard deviations are 0.5 MHz, which is about a factor 5 larger than the stability of the frequency comb (<100 kHz). The source of the fluctuations of the beat note is predominantly due to frequency jitter of the seed laser.

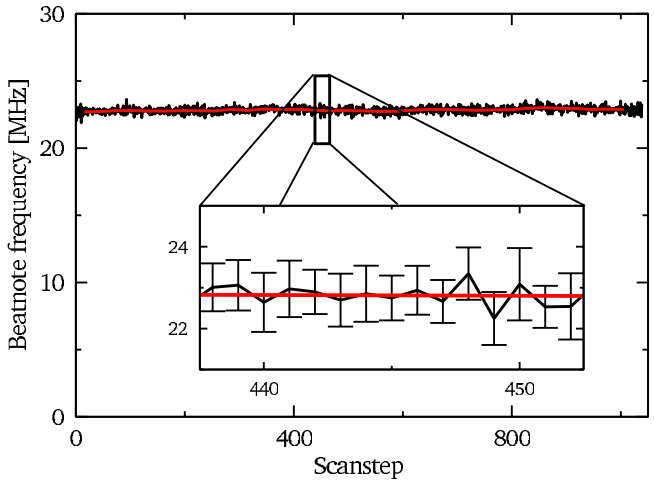

FIG. 6. (Color online) Frequency measurements via counting of ν_{bn} for a scan of 1000 frequency steps.

D. Frequency chirp-induced offset

Since the spectroscopic experiment on the $EF\,^1\Sigma_g^+ \leftarrow X\,^1\Sigma_g^+(0,0)$ transitions is performed with the quadrupled output of the pulsed oscillator (while the frequency calibration procedures are performed on the CW seed-frequency), possible deviations between the two must be considered. Such offsets are common, investigated in detail for traveling-wave dye amplifiers [23–25] and, recently, also for optical parametric oscillators [26,27]. In the present case of a pulsed laser oscillator, containing only a Ti:sapphire crystal as an active optical element inside its resonator (see Fig. 3), the optical path length will depend on the rate of pumping by the Nd:YAG pump laser; a mode-pulling effect will result from the change in refractive index in the Ti:sapphire crystal during the time interval of population inversion.

This phenomenon is assessed experimentally in two steps. First, a possible net average offset between CW and pulsed output is measured using a confocal etalon in an experimental configuration as shown in Fig. 7. Both pulsed and CW beams are overlapped and propagated through a single mode fiber to ensure that they excite a common spatial mode in the etalon. Photodiodes detect fringe traces as in Fig. 7 for both

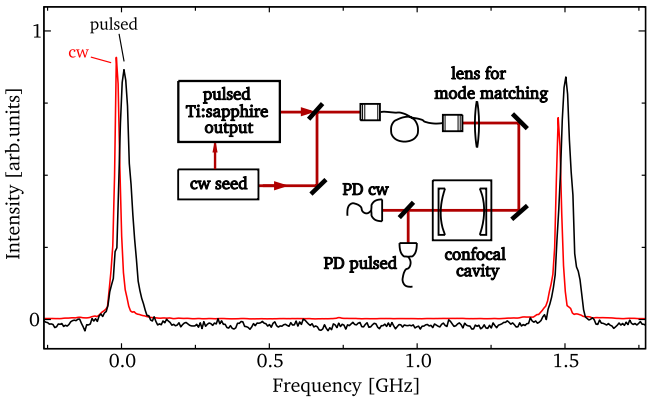

FIG. 7. (Color online) Measurement of the net frequency shift between the output of the CW seed laser and that of the pulsed oscillator (for one specific setting of the Hänsch-Couillaud lock on the cavity). As the seed light is tuned the etalon fringes (FSR =750 MHz) of the pulsed output are redshifted from the CW fringes by 20 MHz. The experimental setup is given as an inlay. Both the pulsed and the CW light are superimposed and mode matched by transmitting them through a single-mode fiber.

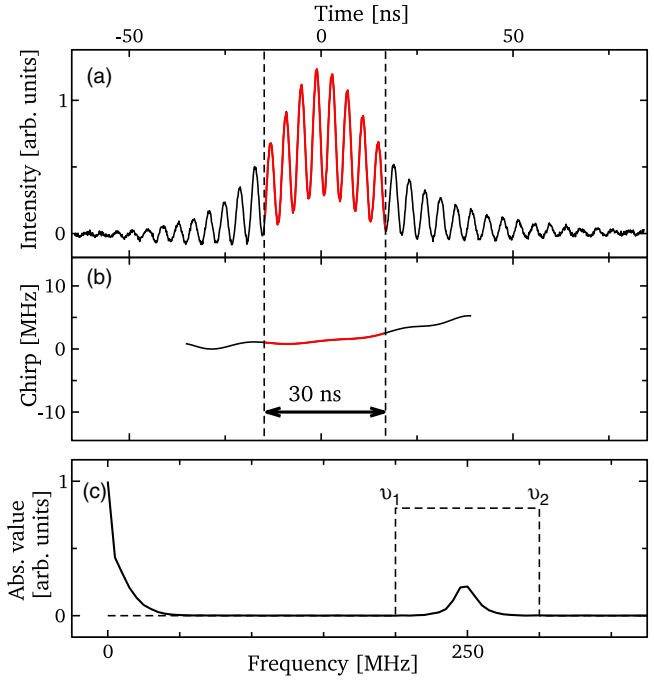

FIG. 8. (Color online) From the beatnote (a) a FFT is performed; (c) shows the corresponding power spectrum. Then the result is filtered and inverse Fourier transformed. From the obtained temporal phase evolution, the instantaneous frequency offset is calculated (b).

the orthogonally polarized signals, when scanning the CW seed frequency and keeping the etalon at fixed free spectral range (FSR). This procedure results in a quantitative value for the average frequency of the pulsed oscillator: its output is redshifted by an amount ≈20 MHz with respect to the CW carrier frequency. We note that this method of chirp detection does not allow for a single pulse assessment of this phenomenon, nor does it produce insight into the frequency excursions during the laser pulse. Rather, it yields an averaged chirp-induced net shift between CW and pulsed outputs of the laser system.

Second, the instantaneous frequency during the temporal evolution of the laser pulse is obtained by heterodyning methods previously described [24–27]. With the use of an acousto-optical modulator (AOM) a CW light field shifted in frequency by 250 MHz is generated from the seed light. This frequency-shifted light is heterodyned with the pulsed light, and the beat note is detected on a fast photodiode detector (New Focus DC-1). For maximum beat-note contrast, the two light fields must be well overlapped, which is achieved by coupling through a single-mode fiber.

The chirp beat note is acquired on a fast oscilloscope (Tektronics TDS 7404; 4 GHz bandwidth, 20 GSample/s)—hereafter referred to as the "chirp scope"—and used to obtain the temporal evolution of the phase $\Phi(t)$, from which the instantaneous frequency is calculated by

$$\nu_{\text{chirp}}(t) = \frac{1}{2\pi}\frac{d}{dt}\Phi(t). \tag{3}$$

In Fig. 8, typical examples of the various steps in the chirp analysis of an acquired beat note are shown.

First the beat-note transient $I(t)$ is Fourier transformed to $\tilde{I}(\nu)$. In this case, the power spectrum [Fig. 8(c)] contains two well-separated peaks. The lower-frequency peak is a result of the envelope of the beat-note signal, and the higher-frequency peak, at ~250 MHz, contains the phase information that allows for calculating a time-dependent change of the instantaneous frequency of the pulse. For extracting the phase information from the beat-note frequency spectrum, the corresponding peak is filtered out by a gate filter $F(\nu) = \Theta(\nu-\nu_1)\Theta(\nu_2-\nu)$, where $\Theta(x)$ is the Heaviside step function [shown in Fig. 8(c)]. The imaginary part of the inverse Fourier-transformed filtered spectrum $\tilde{I}(\nu)F(\nu)$ gives a time-dependent phase $\Phi(t)$ from which the phase evolution due to the AOM frequency has to be subtracted. Finally, the instantaneous frequency differences between the CW carrier and the pulsed output are reconstructed using Eq. (3). The evolution of the instantaneous frequency of the pulsed light can be described as $\Delta_f(t) = \bar{\Delta}_{f_0} + \Delta_{f_0}(t)$, where $\bar{\Delta}_{f_0} = \bar{f}_{\text{out}} - f_{\text{cw}}$ is called the net-pulsed CW frequency offset and $\Delta_{f_0}(t)$ a time-dependent deviation from $\bar{\Delta}_{f_0}$. In Fig. 8, which shows a typical result of the chirp analysis, one can see a shallow slope in $\Delta_f(t)$. The detection and analysis procedures of this dynamic chirp assessment are sufficiently fast to be able to run them online for each individual data point while performing the hydrogen spectroscopic measurements.

An important finding is that the slope of $\Delta_f(t)$ [cf. Fig. 8(b)] can be reduced by lowering the pulse energies to pump the oscillator. Additionally, at low-pump-energy conditions the produced pulses are of longer duration and have a narrower line width. The narrow linewidth and the flat frequency chirp, typically 0–2 MHz on 30 ns, are particularly important for producing nearly Fourier-limited harmonics with a well-defined frequency and will directly reduce the uncertainty budget on the absolute calibration. The lower

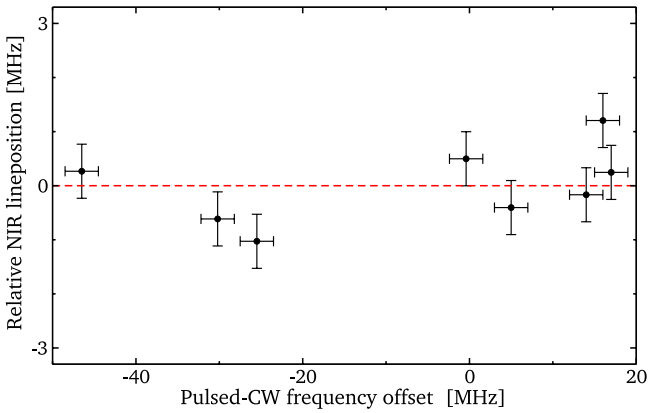

FIG. 9. (Color online) Sequence of spectroscopic scans performed on the $EF \leftarrow X(0,0)$ $Q(1)$ line in H_2 using different chirp frequency offsets ranging from −50 to 20 MHz. The mean value of all acquired positions for the $Q(1)$ line is 99 109.7315 cm^{-1}. The y axis shows the deviations of the line positions of the single scans from that mean value on the infrared frequency scale (around 12 388.7165 cm^{-1}). The standard deviation is 0.7 MHz (cf. discussion in Sec. II D).

pump energy of the pulsed oscillator can be compensated by additional amplification in the multipass amplifier system, when working in the saturated regime. It is verified that at the wavelengths used here, the amplifier changes the temporal evolution of the instantaneous frequency of the output pulses only slightly, which means it shifts the net frequency offset on the order of 2–4 MHz. Therefore, the chirp analysis is performed on the output of the total infrared laser system so that the effect of the amplifier is always taken into account.

In contrast to changes in the pump power, the settings of the Hänsch-Couillaud feedback loop have only little influence on the chirp slope, but strongly affect the frequency offset $\bar{\Delta}_{f_0}$, which, in fact, can be tuned to any value in a range from −50 to 20 MHz. This effect is due to cavity mode pulling: the Hänsch-Coulliaud setting changes the cavity length and, hence, the longitudinal mode structure of the cavity. As a result, the pulsed output is pulled from the seeding frequency toward the closest cavity resonance. In order to check, whether the chirp analysis performs consistently, the $EF \leftarrow X\, Q(1)$ line in H_2 was measured using different chirp offset frequency settings. If the chirp analysis is properly behaved, the transition frequency of the $Q(1)$ line should be independent of the chirp offset. In Fig. 9, the result of a series of scans over the resonance is shown. Each scan obtained at different Hänsch-Couillaud settings. For the resulting different frequency offsets, the fitted transition frequencies are spread around 99 109.7315 cm^{-1} with a standard deviation of 5.6 MHz. Correspondingly, the actual Ti:sapphire frequencies vary around 12 388.7165 cm^{-1} with a standard deviation of 0.7 MHz. It should be noted that both the spread and the mean line position for Fig. 9 are acquired using earlier, preliminary alignment and ionization methods, which where replaced by more accurate procedures afterwards—a Sagnac interferometer replaced a simple retroreflection on a plain mirror and a two-color REMPI replaced a one-color scheme. Correspondingly, the spread in Fig. 9 is a combination of several statistical errors being larger than listed in Table I. It includes larger Doppler uncertainties, larger AC-Stark influences, and more pronounced chirp influences than the ones achieved using the newer methods.

TABLE I. Measured AC-Stark shifts on various $EF\ ^1\Sigma_g^+ \leftarrow X\ ^1\Sigma_g^+(0,0)$ transitions in H_2 and HD.

Molecule	Line	AC-Stark shift [MHz(MW/cm^2)]
H_2	Q(0)	13(7)
	Q(1)	6 (4)
HD	Q(0)	5 (3)
	Q(1)	6 (3)

Though the check in Fig. 9 shows that the actual frequency offset between pulsed and seed light does not affect the final result; the settings were selected such that the offset frequency remains around zero during a scan. In a forthcoming paper, the characteristics of the pulsed laser will be investigated in greater detail. It appears, that the zero-offset setting is also the most efficient for the energy conversion from the cavity pump to the Ti:sapphire near-infrared output. That, in turn, allows for a further reduction of the pump energy and, consequently, a reduction of the chirp. In Fig. 10, the obtained chirp-induced frequency offsets during one spectroscopic scan are displayed for a specific setting of the pump energy for the pulsed oscillator and the Hänsch-Couillaud locking point. As the frequency offset is acquired for ten pulses per scan step, the resulting values are given as ten dots per scan step. From those ten values, the mean value and the standard deviation are calculated. The mean values are shown as the solid line in the figure. They are used for the final frequency calibration of the spectroscopic scan.

For the measurements displayed in Fig. 10 the Hänsch-Couillaud locking was set such that a net shift of $\bar{\Delta}_{f_0}$ is zero.

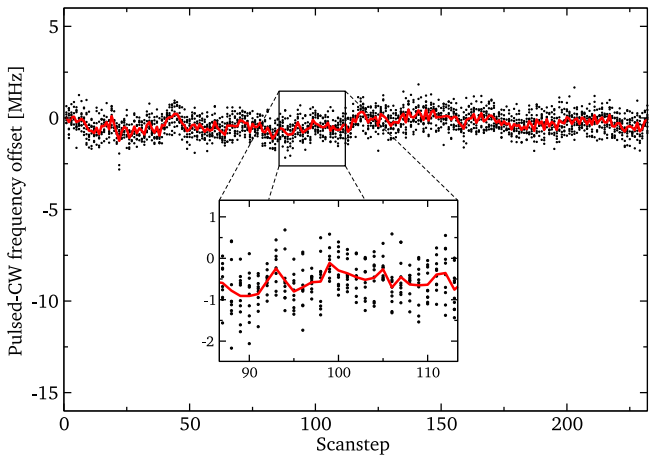

FIG. 10. (Color online) Online chirp analysis for a scan covering ≈260 s at 10 Hz of data for a specific setting of the pump energy for the Ti:sapphire oscillator. The locking point of the Hänsch-Couillaud feedback system was set such that the net shift $\bar{\Delta}_{f_0}$ equals zero.

This is a different setting than used for the data displayed in Fig. 7. It was verified however that the obtained mean values of about −15 to −20 MHz obtained with the etalon method are consistent with the dynamic chirp measurements. The negative sign indicates that the pulsed output has a smaller frequency than the seeding light. The chirp analysis gives information on the relative frequency jitter between seeding light and pulsed output of the Ti:sapphire oscillator.

E. DC and AC-Stark effects

In order to prevent DC-Stark effects from shifting, the transition frequency laser excitation is performed under field-free conditions, while a pulsed extraction voltage ramp (1000 V) is switched 0.3 μs after the excitation to collect the ions produced via (2+1)-REMPI. For the $n=2$ EF state in hydrogen possible stray electric fields at the level below 0.1 V do not affect the transition frequency at the present level of accuracy.

In order to assess the influence of the AC-Stark shift, the output energy of the laser was varied. Finally, the result on each transition frequency is retrieved from an extrapolation to zero pulse energy as shown in Fig. 11. Note that the AC-Stark effect parameter exhibits a different value for each transition. The absolute value for the AC-Stark shift parameter, being 7 MHz/(MW/cm^2) for the $Q(0)$ line in HD, can be determined to within an accuracy of not better than 50% in view of the uncertainties in the measurement of UV pulse energy and the size of the laser beam. The obtained values for the AC-Stark shift parameters are listed in Table II. The present value for the AC-Stark parameter pertaining to the Q(1) line of H_2 is in reasonable agreement with that of Vrakking *et al.* [32], who found 15 MHz/(MW/cm^2).

For the determination of AC-Stark free transition frequencies, the extrapolations to zero intensities are relevant, irrespective of the absolute pulse intensity scale. In a first round of experiments, the absolute transition frequencies of most lines were determined from such extrapolations of the measured frequencies in the one-color (2+1)-REMPI scheme. A general result from the entire set of measurements on the assessment of the AC-Stark effect is that at the lowest laser intensities, corresponding to pulse energies (<4 μJ), the AC-Stark shifts are <1 MHz. Hence, a second round of measurements was performed on all lines in H_2, HD, and D_2 in which the excitation laser was kept below 4 μJ/pulse and where the ionization was accomplished by a second intense UV laser pulse (at 355 nm) that was temporally delayed by ≈50 ns. In this two-color REMPI scheme, AC-Stark free measurements were performed resulting in the most accurate values for the transition frequencies. It was verified that the data of the extrapolated one-color experiments are consistent with those of the two-color pulse-delayed scheme.

F. Phase distortions in nonlinear mixing

Additional effects of frequency chirp can be induced as a result of optical phase distortions in the processes of nonlinear mixing for the generation of harmonics. These issues and the consequences for frequency metrology on the basis of

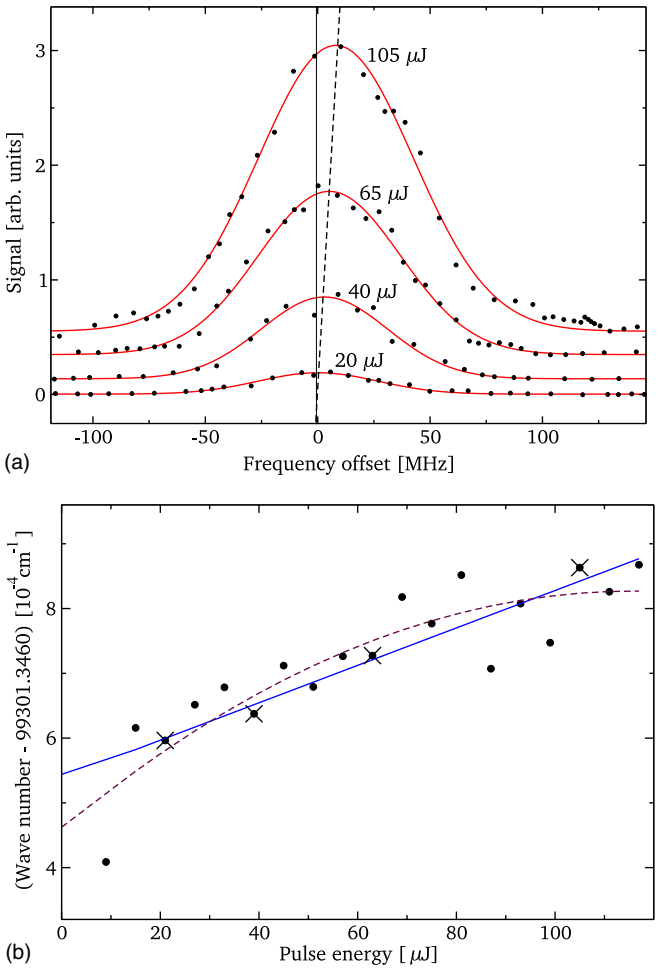

FIG. 11. (Color online) Assessment of the AC-Stark effect on the $EF\ ^1\Sigma_g^+ \leftarrow X\ ^1\Sigma_g^+(0,0)$ $Q(0)$ line in HD by measurement of the transition frequency as a function of laser pulse energy with parameters: pulse length 12 ns (at 202 nm) and collimated beam diameter of 0.04 cm. The upper graph shows data obtained at four different pulse energies for the deep-UV excitation laser, here used in the 2+1 one-color REMPI scheme. The line positions found for different data traces in the upper graph are marked with a × in the lower graph. Extrapolation by linear regression to the intercept yields a value of 99 301.346 54(6) cm^{-1} for this specific measurements series and a value for the AC-Stark shift of 7 MHz/(MW/cm^2). A quadratic regression (dashed line) leads to an intercept of 99 301.346 46(6) cm^{-1}.

pulsed laser sources were discussed in detail by Gangopadhyay *et al.* [33] Firstly, the optical Kerr effect, modulating the index of refraction $n(t)$ with the laser intensity $I(t)$ during the pulse evolution via $n(t)=n_0+n_{\mathrm{Kerr}}I(t)$, may give rise to phase distortions of the size [33,34]:

$$\phi(t) = -\frac{2\pi L n_{\mathrm{Kerr}} I(t)}{\lambda}, \tag{4}$$

where L is the length of the nonlinear crystal, λ the wavelength, and n_{Kerr} the wavelength-dependent Kerr index for the used crystal.

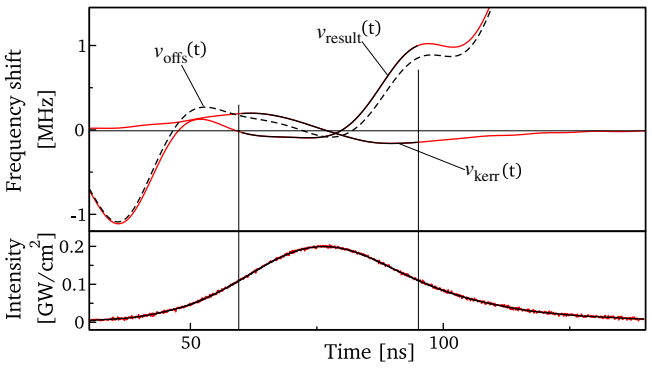

FIG. 12. (Color online) The influence of the Kerr effect on the instantaneous frequency evolution in the SHG crystal calculated for a typical infrared pulse of 0.2 GW/cm^2 peak intensity and 35 ns duration. ν_{offs}: pulsed-CW frequency offset measured in front of the SHG crystal, ν_{kerr}: instantaneous frequency shift caused by the Kerr effect, ν_{result}: the sum of ν_{offs} and ν_{kerr}.

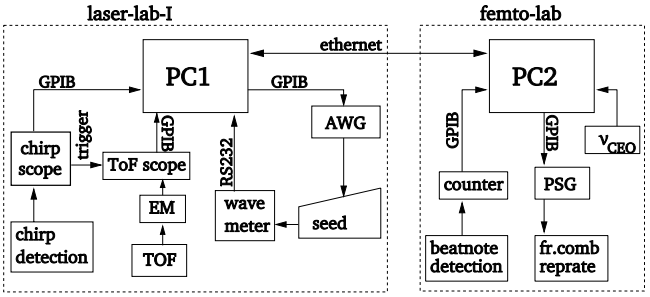

FIG. 13. Flow control scheme and overview of the experimental components. PC1 is the master system, taking control of the laser scan and requesting data from frequency comb server PC2 in the femtolab. PC2 initiates the beat-note counts, but also maintains the beat note within a frequency window by controlling the repetition rate of the comb. AWG: arbitrary wave-form generator. DAC: GPIB signal acquisition interface. PSG: signal generator. ν_{ceo}: the carrier-envelope offset frequency is entered into the data acquisition manually.

The resulting chirp may be evaluated via Eq. (3). The Kerr index of beta-barium borate (BBO) has been measured by Li *et al.* [35] at 1064 and 532 nm at different crystal axes. The obtained values vary between 4×10^{-16} cm^2/W and 5×10^{-16} cm^2/W and are given with a 20% error margin. For the moment, the analysis is restricted to the Kerr effects induced in the stage of the second harmonic generation (SHG). In Fig. 12, an example for typically used infrared pulse intensities of 0.2 GW/cm^2 in the SHG crystal is calculated. For obtaining the temporal intensity profile $I(t)$, shown in Fig. 12(b), the normalized signal of a fast photodiode (Thor labs DET210) with a response time of 1 ns was used. Using the chirp analysis system, the corresponding instantaneous frequency evolution $\nu_{offs}(t)$ in the SHG crystal was acquired and is displayed in Fig. 12(a). From the calculation using Eq. (4) inserted into Eq. (3), it is apparent that the Kerr effect modulates the instantaneous frequency ν_{result} in an antisymmetric way around the maximum of $I(t)$. At the rising side, the instantaneous pulse frequency is shifted to higher frequencies and, at the falling side, to negative frequencies. Possible deviations from a perfect antisymmetric behavior resulting from an asymmetric temporal pulse profile $I(t)$ could produce net frequency shifts affecting the absolute calibration. Based on a simulation the net frequency shift, $\bar{\Delta}_{f_0}$ was calculated both with an without the Kerr effect. As a result of the nearly antisymmetric evolution of $\nu_{Kerr}(t)$, the difference between the two net shifts proved to be insignificant, as the net Kerr shift is several orders of magnitude below the uncertainties of the chirp analysis of Sec. II D.

The fact that the instantaneous effect of the Kerr-induced phase distortions is quasi-antisymmetric over the temporal profile of the pulse, and also for the subsequent stages of third and fourth harmonic generation their net effect on the frequency calibration is far below other sources of calibration uncertainties. In principle, at the following sum frequency mixing stages, the Kerr effect could indeed cause frequency shifts, when a time delay between the two contributing input beams was introduced. However with typical pulse lengths of 20 ns as used here, careful alignment of the lengths of the beam branches in the upconversion stages efficiently prevents such problems.

A second phenomenon resulting in chirp from phase distortions in nonlinear mixing is associated with a deviation from optimum phase matching [33,36]. We decided to assess the effects of nonperfect phase matching via an experimental approach. The entire optical layout, in particular involving the alignment of the beam propagation and the adjustment of the phase-matching angles, was set up from scratch in a number of separated measurement days focusing on a few transitions. After the complete daily realignment procedure, both the phase-matching angles of the upconversion crystals and the dark fringe at the exit port of the Sagnac interferometer were readjusted for each single scan. During those procedures, indeed, statistical day-to-day excursions in the determined transition frequencies were obtained with a standard deviation of about 2.5–6 MHz, depending on the isotopic species and particular line; these excursions are somewhat larger than the 1σ spread of results obtained during a measurement series of one day, which was limited to 2–3 MHz. These excursions are attributed to the combined effect of Doppler shifts, phase distortions in nonlinear mixing, day-to-day beam-profile variations, and varying wavefront distortions. Particularly, the latter two effects are more dependent on the daily full realignment of the optical layout.

G. Integrated setup and measurement procedures

The three different laser systems—the CW Ti:sapphire seed laser and the Ti:sapphire pulsed oscillator-amplifier system in one laboratory, the frequency comb lasers in another laboratory separated by 100 m, and the vacuum and detection equipment—are assembled into one experiment of which a schematic overview is shown in Fig. 13. In laser-lab-I, where the spectroscopic data are recorded, master computer PC1 takes control of all tasks during the experiment. The frequency of the seed laser is driven, via its external voltage scan port, by an arbitrary wave-form generator (Agilent AWG 33250A) connected via GPIB to PC1. The "chirp

scope" is triggered by a photodiode detecting the 202 nm light. The sample beat-note wave forms (as in Fig. 8) are transferred via GPIB to PC1, where the chirp analysis is carried out. Finally, the REMPI-TOF signal is registered on an electron multiplier tube and digitally integrated using a LeCroy WaveRunner oscilloscope (the "TOF scope"). The TOF scope is triggered by the external trigger interface of the chirp scope. This combined trigger acquisition ensures that all possible data are acquired from each pulse following the 10 Hz repetition rate of the laser: the chirp parameters, the relative UV power, and the REMPI signal. This pulse-correlated acquisition allows for using binning and filtering techniques for data analysis, some of which are performed off-line. By this means, correlations between power fluctuations of the pump laser, the chirp and frequency-pulling characteristics, and the UV output power can be investigated. Also, the AC-Stark-induced frequency shifts resulting from UV power fluctuations can be used to derive the AC-Stark parameter.

In the femtolab (cf. Fig. 13), where the frequency comb is operated, PC2 is responsible for the frequency-comb laser control and data acquisition. The beat-note signal detected on the avalanche photodiode (Fig. 5) is filtered via a RF bandpass filter to remove signal from higher-order beat notes, amplified, processed via a discriminator and counted on a frequency counter (Agilent 53132A Universal Counter) connected to PC2 via GPIB. The repetition rate of the frequency comb—actually, its 140th harmonic—is locked to a frequency of ~10 GHz. This frequency is generated by a radiofrequency synthesizer (Agilent PSG-L F8241A), which is locked to a Rubidium clock standard. The set frequency of the synthesizer is controlled by PC2 via GPIB bus. In order to maintain synchronous operation in the two labs, PC2 stays in connection with PC1 via a server client protocol running on top of the Ethernet™. PC2 initiates beat-note counting on PC1's request. Furthermore PC2, depending on the actual beat-note readout, adjusts the repetition rate of the frequency comb in order to maintain the beat note within a frequency window of 21–24 MHz, which is the working range of the final low-pass filter in front of the frequency counter.

The wavelength of the seed light is continuously monitored by an ATOS LM 007 wave meter and sent to PC1 through a RS 232 serial connection. Although its long-term stability is ~30 MHz in the near infrared, during the time span of an experiment it remains reproducible to within 3 MHz. This auxilliary instrument is used for precalibration, for detection of possible mode hops of the CW seed laser and for establishing the sign of the beat-note frequency between frequency comb and seed light.

The experimental procedure is as follows: After the precalibration is finished using iodine saturation spectroscopy (cf. Fig. 4), the actual frequency-comb measurement is performed. First, the seed laser is tuned to the start frequency, which is chosen to be ~30 MHz removed from the two-photon resonance. Then the repetition rate of the frequency comb is set such that the beat-note frequency between seed and frequency comb is 22±2 MHz (within the accepted range of the bandpass filter in use). Furthermore, the sign of the beat-note frequency must be established. Then, the scan is started: using the AWG connected to PC1, the laser is scanned with a fixed voltage step per scan step. On each scan step the beat-note frequency between seed and frequency comb is counted. If the frequency comb would run at fixed settings and no bandpass filter was used, depending on the sign of the beat-note frequency, the beat-note frequency would increase until reaching half the repetition rate ν_{rep} and decrease again, or it would decrease until a zero beat note is reached and then increase again. In order to avoid inevitable assignment problems at beat-note frequencies close to zero or $\nu_{rep}/2$, the beat note is quasi-locked around the start value. This is achieved by steadily adjusting ν_{rep} at each scan step after finishing the beat-note frequency counting.

Each scan covers a range of ~70 MHz (in the near infrared) and consists of ~300 equidistant voltage steps. On each step, PC1 first requests PC2 to start the beat-note frequency counting in the femtolab. Then the chirp scope and TOF scope are triggered ten times so that the data of ten pulses are obtained. Next, PC1 requests PC2 to send all relevant data from the frequency comb, ν_{rep}, ν_{ceo}, and ν_{bn}. The software written on both computers is based on the PYTHON programing language. The mathematically more involved part of the chirp analysis is written using the SCIPY [37] package.

TABLE II. (A) Estimated systematical error budget for the frequency calibrations of the $EF\ ^1\Sigma_g^+ \leftarrow X\ ^1\Sigma_g^+(0,0)$ transitions in hydrogen. (B) The experimentally obtained statistical spread listed for each line.

(A) Systematics detail		Value (MHz)
(i) Doppler	H_2	0.75
	HD	0.6
	D_2	0.5
(ii) Calibration	Frequency comb	<0.1
(iii) Chirp	In Ti:sapphire oscillator	2
(iv) Chirp	In nonlinear mixing	<0.01
(v) AC Stark	In two-color scheme	<1.0
Estimated systematical error budget[a]		3.2
(B) Statistics[b]	H_2 Q(0),Q(2)	3.3
	H_2 Q(1)	5.4
	HD Q(0),Q(1)	6.0
	D_2 Q(0),Q(1)	2.4
	D_2 Q(2)	2.1

[a]Quadrature summation of errors (i–iv) and adding (v) linearly to the result.

[b](1σ) standard deviation of all results (10–15 scans per line) obtained over several days.

H. Uncertainty budget for transition frequencies

In this section, the final contributions to the uncertainty budget for the present calibration study on $EF\ ^1\Sigma_g^+ \leftarrow X\ ^1\Sigma_g^+(0,0)$ lines are compiled. The estimated values, discussed extensively in the previous sections are listed in Table II. The major contributions are associated with the chirp characteristics of the pulsed oscillator (documented in Sec.

TABLE III. The two-photon energy values in various hydrogen isotopomers for $EF\ ^1\Sigma_g^+ \leftarrow X\ ^1\Sigma_g^+(0,0)$ transitions and a comparison with results by Yiannopoulou *et al.* [19] Δ represents the deviation between presently obtained values and those of Yiannopoulou *et al.* [19] The numbers given in parentheses in column 3 are the final estimates of the uncertainty as discussed in Sec. II H.

Species	Line	This work (cm^{-1})	Ref. [19] (cm^{-1})	Δ (cm^{-1})
H_2	Q(0)	99 164.786 91(11)	99 164.7871(8)	−0.0002
	Q(1)	99 109.731 39(18)	99 109.7316(8)	−0.0002
	Q(2)	99 000.183 01(11)		
HD	Q(0)	99 301.346 62(20)	99 301.3461(8)	+0.0005
	Q(1)	99 259.917 93(20)	99 259.9184(8)	−0.0005
D_2	Q(0)	99 461.449 08(11)	99 461.4490(8)	+0.0001
	Q(1)	99 433.716 38(11)	99 433.7166(8)	−0.0002
	Q(2)	99 378.393 52(11)	99 378.3937(8)	−0.0002

II D) and with the nonperfect overlap of the two counterpropagating laser beams pumping the two-photon resonance. In the present experiment, an almost negligible uncertainty is associated with the absolute frequency scale by using a frequency-comb laser. The estimate on the AC-Stark effect pertains to the two-color (2+1)-REMPI scheme, in which pulse energies of <4 μJ are used for the two-photon excitation. The resulting final estimate for the uncertainty of a transition frequency, including all systematics is evaluated at 3.2 MHz. The statistical spread (1σ) in the data for measurements recorded under identical conditions on the same day is limited to 2 MHz for H_2 and D_2 and to 3 MHz for HD—for the latter, lower beam densities were applied yielding lower s/n ratios. These uncertainties are consistent with the final systematic estimate as listed in Table I. However, the spread (1σ) over varying conditions of several days measurements can be as large as 5.4 MHz for H_2 $Q(1)$ and 6 MHz for HD (cf. Table I), but is smaller in other cases. We do not know the exact origin of these somewhat larger variations. Since the known sources of systematic uncertainties lead to a smaller value, the day-to-day variations are treated as statistical uncertainties. In the final listing of the transition frequencies in Table III, the estimated systematical error budget of 3.2 MHz or 0.00011 cm^{-1} (Table I) is considered as lower uncertainty limit.

One possible contribution to statistical variation not discussed thus far is the nonlinear curve fitting for obtaining the line positions. In the present study, we have not elaborated on line-shape models because all spectral lines, recorded at low intensity, could be fitted to purely Gaussian line profiles. A typical example of a recorded line is shown in Fig. 14. Each scan consists of about 2000–3000 datapoints and spans about 300 MHz at the two-photon level. The obtained fitting uncertainties for the line center positions are ~0.4 MHz for each single scan and all measured lines, which is to small to explain the descrepancy between estimated error budget and experimentally observed spread.

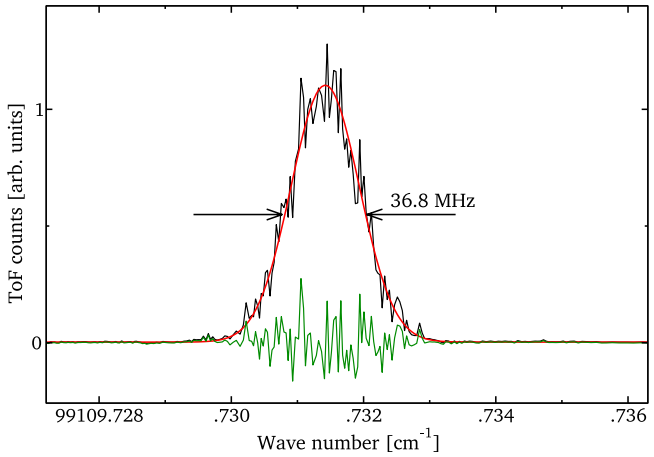

FIG. 14. (Color online) Scan on the $EF\ ^1\Sigma_g^+ \leftarrow X\ ^1\Sigma_g^+(0,0)$ $Q(1)$ line in H_2. This spectrum was recorded under low-pulse-energy pumping conditions for the Ti:sapphire pulsed oscillator delivering the narrowest bandwidth output. Each datapoint represents an average over ten shots. The linewidth obtained in this spectrum is 36.8 MHz. The smooth line corresponds to a Gaussian function fitted to the observed spectral data; residuals are shown as well.

III. RESULTS AND CONCLUSIONS

The present study involves a highly accurate frequency measurement of eight spectral lines in the $EF\ ^1\Sigma_g^+ \leftarrow X\ ^1\Sigma_g^+(0,0)$ band of H_2, HD, and D_2 by Doppler-free two-photon excitation in the collision-free conditions of a molecular beam. As a typical example, in Fig. 14 a scan over the $Q(1)$ line in H_2 under conditions of a narrowband excitation pulse in the two-color (2+1)-REMPI scheme is shown. Resulting values for the transition frequencies are listed in Table III. Values for the AC-Stark shift were derived and are given in Table II. In the two-color REMPI scheme, the AC-Stark effect was reduced to a submegahertz level. An absolute accuracy of 2×10^{-9} on the transition frequencies is achieved, thanks to the implementation of several technologies. A pulsed Ti:sapphire oscillator laser was designed to produce Fourier-transform limited narrowband pulses of which the chirp was measured on-line at high precision. A frequency comb, referenced to a Rb-atomic clock and to the GPS, was implemented in a spectroscopic measurement chain for calibrating chirp-controlled nanosecond pulses.

The present results are in excellent agreement with a previous set of measurements on the same lines, performed at the 8×10^{-9} accuracy level. It is important to note that the study of Yiannopoulou *et al.* [19] involves an entirely different setup and measurement procedures. Hence, it is more than comforting that the deviations between the two experiments are much less than expected based on the quoted uncertainties. The combined results of the present study and those of Yiannopoulou *et al.* [19] form an essential ingredient for a future determination of a value of the ionization potential in H_2 and the other hydrogen isotopomers at an accuracy of 0.001 cm^{-1}.

ACKNOWLEDGMENTS

We thank H. Knöckel (Hannover) for lending us a cell to perform I_2 saturation spectroscopy in the near-infrared region, and E. E. Eyler (Connecticut) for discussing results obtained by his group prior to publication. The Netherlands Foundation for Fundamental Research on Matter (FOM) is gratefully acknowledged for financial support.

[1] E. E. Eyler, Comments At. Mol. Phys. **24**, 299 (1990).
[2] B. P. Stoicheff, Can. J. Phys. **79**, 165 (2001).
[3] W. Kołos, J. Chem. Phys. **101**, 1330 (1994).
[4] L. Wolniewicz, J. Chem. Phys. **103**, 1792 (1995).
[5] A. Balakrishnan, V. Smith, and B. P. Stoicheff, Phys. Rev. Lett. **68**, 2149 (1992).
[6] E. F. McCormack and E. E. Eyler, Phys. Rev. Lett. **66**, 1042 (1991).
[7] Y. P. Zhang, C. H. Cheng, J. T. Kim, J. Stanojevic, and E. E. Eyler, Phys. Rev. Lett. **92**, 203003 (2004).
[8] G. M. Greetham, U. Hollenstein, R. Seiler, W. Ubachs, and F. Merkt, Phys. Chem. Chem. Phys. **5**, 2528 (2003).
[9] A. de Lange, E. Reinhold, and W. Ubachs, Phys. Rev. A **65**, 064501(R) (2002).
[10] C. Jungen, I. Dabrowksi, G. Herzberg, and M. Vervloet, J. Chem. Phys. **93**, 2289 (1990).
[11] D. W. Chandler and L. R. Thorne, J. Chem. Phys. **85**, 1733 (1986).
[12] W. L. Glab and J. P. Hessler, Phys. Rev. A **35**, 2102 (1987).
[13] E. E. Eyler, J. Gilligan, E. McCormack, A. Nussenzweig, and E. Pollack, Phys. Rev. A **36**, 3486 (1987).
[14] E. McCormack, J. M. Gilligan, C. Cornaggia, and E. E. Eyler, Phys. Rev. A **39**, 2260 (1989).
[15] J. M. Gilligan and E. E. Eyler, Phys. Rev. A **46**, 3676 (1992).
[16] D. Shiner, J. M. Gilligan, B. M. Cook, and W. Lichten, Phys. Rev. A **47**, 4042 (1993).
[17] M. Vervloet and D. Bailly (private communication).
[18] A. Osterwalder, A. Wuest, F. Merkt, and C. Jungen, J. Chem. Phys. **121**, 11810 (2004).
[19] A. Yiannopoulou, N. Melikechi, S. Gangopadhyay, J. C. Meiners, C. H. Cheng, and E. E. Eyler, Phys. Rev. A **73**, 022506 (2006).
[20] M. Sneep, S. Hannemann, E.-J. van Duijn, and W. Ubachs, Opt. Lett. **29**, 1378 (2004).
[21] R. T. Zinkstok, S. Witte, W. Ubachs, W. Hogervorst, and K. S. E. Eikema, Phys. Rev. A **73**, 061801(R) (2006).
[22] S. Witte, R. T. Zinkstok, W. Ubachs, W. Hogervorst, and K. S. E. Eikema, Science **307**, 400 (2005).
[23] M. S. Fee, K. Danzmann, and S. Chu, Phys. Rev. A **45**, 4911 (1992).
[24] N. Melikechi, S. Gangopadhyay, and E. E. Eyler, J. Opt. Soc. Am. B **11**, 2402 (1994).
[25] K. S. E. Eikema, W. Ubachs, W. Vassen, and W. Hogervorst, Phys. Rev. A **55**, 1866 (1997).
[26] R. T. White, Y. He, B. J. Orr, M. Kono, and K. G. H. Baldwin, J. Opt. Soc. Am. B **21**, 1577 (2004).
[27] R. T. White, Y. He, B. J. Orr, M. Kono, and K. G. H. Baldwin, Opt. Lett. **28**, 1248 (2004).
[28] S. Hannemann, E. J. Salumbides, S. Witte, R. T. Zinkstok, E.-J. van Duijn, K. S. E. Eikema, and W. Ubachs, Phys. Rev. A **74**, 012505 (2006).
[29] T. W. Hänsch and B. Couillaud, Opt. Commun. **35**, 441 (1980).
[30] D. Shiner, J. M. Gilligan, B. M. Cook, and W. Lichten, Phys. Rev. A **47**, 4042 (1993).
[31] Database and program for calculating absolute frequencies of hyperfine components in the I_2 saturation spectrum kindly provided by Dr. Knöckel, the University of Hannover; see also: H. Knöckel, B. Bodermann, and E. Tiemann, Eur. Phys. J. D **D28**, 199 (2004).
[32] M. J. J. Vrakking, A. S. Bracker, T. Suzuki, and Y. T. Lee, Rev. Sci. Instrum. **64**, 645 (1993).
[33] S. Gangopadhyay, N. Melikechi, and E. E. Eyler, J. Opt. Soc. Am. A **11**, 231 (1994).
[34] R. W. Boyd, *Nonlinear Optics* (Academic, New York, 1992).
[35] H. Li, F. Zhou, X. Zhang, and W. Ji, Opt. Commun. **144**, 75 (1997).
[36] R. DeSalvo, D. J. Hagan, M. Sheik-Bahae, G. Stegeman, E. W. van Stryland, and H. Vanherzelle, Opt. Lett. **17**, 2 (1992).
[37] SciPy: Open source scientific tools for Python, E. Jones, T. Olifant, P. Peterson *et al.*, http://www.scipy.org/ (2000).